Spatial vibrations suppressing resonant tunneling

Gilad Zangwill ● and Er'el Granot

Department of Electrical and Electronics Engineering, Ariel University, Ariel

The dynamics of resonant tunneling via a spatially oscillating narrow well is investigated. The well generates a quasiresonance state, which can trap the incoming particles. Four spectral regimes are found: (1) the adiabatic regime, when the vibrations' frequency is lower than the spectral width of the resonance. In this regime, the mean current is independent of the vibration's frequency, and the current decreases as a function of the vibration's amplitude. (2) When the frequency of the vibration is higher than the spectral width of the resonance, the particle is partially trapped to the moving well and the dependence of the current on the vibrations' amplitude is more moderate. (3) However, *and this is the main result of this paper*, beyond a certain frequency the kinetic energy of the trapped particle exceeds the spectral width of the resonance, in which case particles cannot be trapped in the moving well and the current is abruptly suppressed. (4) When the energy quanta of the vibrations are higher than the energy gap between the resonance energy and the barrier's potential height, a single phonon can be absorbed by the particle only when the final energy agrees with the resonances of the barrier, in which case current suppression is selective and occurs only for specifics frequencies. The model is solved exactly numerically, and analytical approximations are presented for the different regimes. The analytical solutions show high agreement with the numerical ones. This effect can be implemented in extremely sensitive accelerometers. Moreover, it may explain the odor receptor's sensitivity to molecular vibrations.

I. INTRODUCTION

Quantum tunneling is a fascinating phenomenon, which appears in a broad range of scientific disciplines: the foundation of quantum physics [1–16], nanoelectronics and nanotechnology [17–20], and even in biology and biochemistry [21–35]. In ordinary quantum tunneling, particles can propagate through a classically impenetrable potential barrier. This process occurs with a very low probability, which is exponentially small when the barrier is high and wide. However, when a quasibound state is formed within the barrier, and the particle's energy is close to this resonance energy (i.e., to the quasibound state's energy), then the particle's transmission probability increases substantially. This effect is known as resonant tunneling (RT) [1–5,14]. When the potential well is time dependent, a wealth of physical phenomena appear. On the one hand, activation and elevation effects appear [7–8,11,13–14], but on the other hand, selected *suppression* of activation and the Sisyphus effect appear as well [11–14,16].

Besides the academic interest in these complex processes, these effects were suggested to be implemented in extremely sensitive nanodevices (such as in nanotransistors). Moreover, some interesting evidence suggests that dynamic RT is a fundamental ingredient in bioquantum mechanics in general, and the olfactory mechanism of odor detection in particular [23–28].

However, if the source of the oscillations is mechanical vibrations rather than potential variations, e.g., when a molecule vibrates inside a receptor or when a particle oscillates in an accelerometer, then the models of Refs [11,13,14,24,26] fail to examine the system.

In the literature, δ function potential was used extensively to simulate localized potential wells [15,35–39]. Consequently, the simplest approach to simulate an oscillating local potential is to use an oscillating δ function [3,7–8,10–14,16,40,41].

In this paper, we investigate the RT current via a spatially oscillating local well, which vibrates inside an opaque potential barrier.

Since only the position of the well is oscillating, then except for exponentially small variations, the resonant energy is almost unchanged. We therefore take the incoming particle's energy to be equal to this resonant energy (otherwise the particles cannot be trapped by the well). Consequently, unless the oscillations' frequency is of the same order of magnitude as the barrier's energy, the particle's energy is almost unaltered.

The illustration of the system is depicted in Fig. 1. To simplify the analysis, we choose a rectangular barrier and a δ function well. However, a δ function is an excellent approximation for a well, whose width is narrower than the de Broglie wavelength of its bound state [4]. Therefore, the well is characterized by its bound-state de Broglie wavelength λ, the oscillations' amplitude a, and frequency ω.

Moreover, since this is a scattering process, and scattering occurs between eigenstates, then as long as the incoming particles' energy is approximately equal to the well's resonant state, the effect will be the same even for differently shaped wells. Therefore, the conclusions that can be drawn from the δ function well are valid for other shapes of the well.
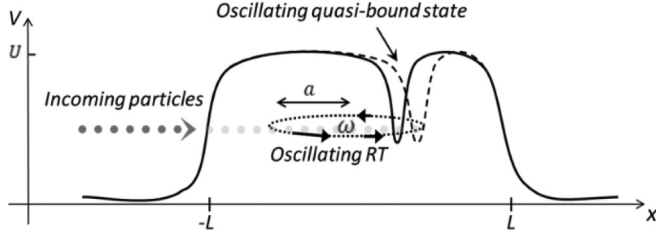
FIG. 1. An illustration of the system: the incoming particles' energy is exactly equal to resonance energy. The barrier height is U and its width is $2L$. The quasibound state oscillates spatially with frequency ω and amplitude a.

II. THE MODEL AND ITS GENERIC SOLUTION

The Schrödinger equation of the system, which is presented in Fig. 1, can be written as

$$\left\{-\frac{\partial^2}{\partial x^2} + U(x) - \lambda\delta[x - a\cos(\omega t)]\right\}\psi(x,t) = i\frac{\partial}{\partial t}\psi(x,t), \quad (1)$$

where we have used the units $\hbar = 1$ and $2m = 1$ (m is the electrons' mass). $U(x)$ is the barrier potential, a is the amplitude of the vibration, and ω is the frequency of the vibration.

The solution can be written as a superposition of propagating waves: on the left side of the well,

$$\psi_l(x < a\cos(\omega t), t) = \varphi_\Omega^+(x)e^{-i\Omega t}$$
$$+ \sum_{m=-\infty}^{\infty} r_m \varphi_{\Omega+m\omega}^-(x)e^{-i(\Omega+m\omega)t}, \quad (2)$$

and on its right side,

$$\psi_r(x > a\cos(\omega t), t) = \sum_{m=-\infty}^{\infty} t_m \varphi_{\Omega+m\omega}^+(x)e^{-i(\Omega+m\omega)t}, \quad (3)$$

where $\varphi_\Omega^+(x)\exp(-i\Omega t)$ and $\varphi_\Omega^-(x)\exp(-i\Omega t)$ are the homogeneous solutions of Eq. (1), i.e., the solutions of the equation without the well, while $\varphi_\Omega^+(x)$ and $\varphi_\Omega^-(x)$ solve the stationary-state equation:

$$-\frac{\partial^2\varphi_{\Omega+m\omega}^\pm(x)}{\partial x^2} + [U(x) - (\Omega + m\omega)]\varphi_{\Omega+m\omega}^\pm(x) = 0. \quad (4)$$

The subscripts "l" and "r" stand for "left" and "right," respectively. Continuity conditions at $x = a\cos(\omega t) \equiv x_0$ require

$$\psi_l(x_0, t) = \psi_r(x_0, t), \quad (5)$$

$$\psi_l'(x_0, t) - \psi_r'(x_0, t) = -\lambda\psi(x_0, t), \quad (6)$$

where the tags represent spatial derivatives. Substitution of (2) and (3) into (5) and (6) yields

$$\varphi_\Omega^+(x_0)e^{-in\omega t} = -\sum_m r_m \varphi_{\Omega+m\omega}^-(x_0)e^{-i(m+n)\omega t}$$
$$+ \sum_m t_m \varphi_{\Omega+m\omega}^+(x_0)e^{-i(m+n)\omega t} \quad (7)$$

and

$$\varphi_\Omega'^+(x_0)e^{-in\omega t} = -\sum_m r_m \varphi_{\Omega+m\omega}'^-(x_0)e^{-i(m+n)\omega t}$$
$$+ \sum_m t_m [\varphi_{\Omega+m\omega}'^+(x_0) - \lambda\varphi_{\Omega+m\omega}^+(x_0)]e^{-i(m+n)\omega t}. \quad (8)$$

The wave functions inside the barrier zone can be written as

$$\varphi_{\Omega+m\omega}^+[x = a\cos(\omega t)] = Ce^{-K_m a\cos(\omega t)} + De^{K_m a\cos(\omega t)}, \quad (9)$$

$$\varphi_{\Omega+m\omega}^-[x = a\cos(\omega t)] = Ce^{K_m a\cos(\omega t)} + De^{-K_m a\cos(\omega t)}, \quad (10)$$

where $k_m \equiv \sqrt{\Omega + m\omega}$ and $K_m \equiv \sqrt{U - k_m^2}$, and the coefficients C and D are [1]

$$C = \frac{F}{2}\left(1 - i\frac{k_m}{K_m}\right)e^{K_m L + ik_m L}, \quad (11)$$

$$D = \frac{F}{2}\left(1 + i\frac{k_m}{K_m}\right)e^{-K_m L + ik_m L}, \quad (12)$$

respectively, where

$$F = \left[\cos h(2K_m L) + \frac{i\varepsilon}{2}\sinh(2K_m L)\right]^{-1} e^{-i2k_m L} \quad (13)$$

and $\varepsilon = \frac{K_m}{k_m} - \frac{k_m}{K_m}$.

Making use of the integral identity [42,43]

$$\int_0^{2\pi/\omega} e^{i[Ka\cos(\omega t) - m\omega t]} \, dt = \frac{2\pi}{\omega} i^m J_m(Ka) \quad (14)$$

and limiting the number of modes to $2N + 1$, we find the following set of linear equations for r_m and t_m:

$$J_n(iK_0 a)[C + D(-1)^n]$$
$$= \sum_{m=-N}^{+N} i^m J_{m+n}(iK_m a)\{[C(-1)^{m+n+1} - D]r_m$$
$$+ [C + D(-1)^{m+n}]t_m\} \quad (15)$$

and

$$K_0 J_n(iK_0 a)[-C + D(-1)^n]$$
$$\sum_{m=-N}^{+N} i^m J_{m+n}(iK_m a)[K_m[C(-1)^{m+n+1} + D]r_m$$
$$= +\{K_m[-C + D(-1)^{m+n}] - \lambda[C + D(-1)^{m+n}]\}t_m], \quad (16)$$

where $K_0 \equiv \sqrt{U - \Omega}$.

Equations (15) and (16) can be written in a simpler matrix form:

$$\begin{bmatrix} M_1 & M_2 \\ M_3 & M_4 \end{bmatrix}\begin{bmatrix} \mathbf{r} \\ \mathbf{t} \end{bmatrix} = \begin{bmatrix} \mathbf{V_1} \\ \mathbf{V_2} \end{bmatrix}, \quad (17)$$
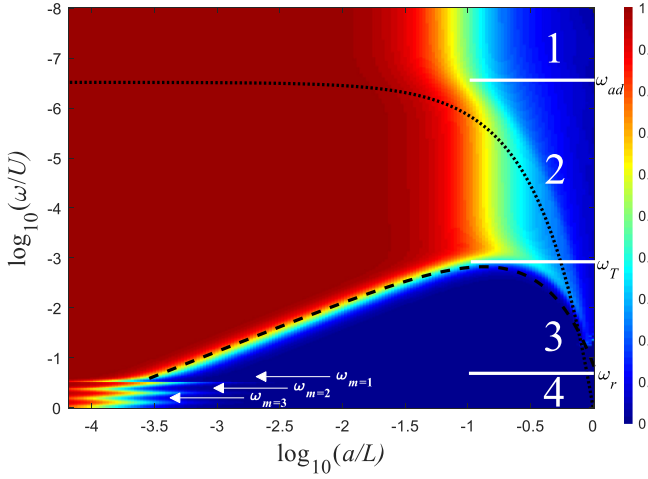
FIG. 2. A false-color presentation of the exact numerical solution of the average current density $\langle j \rangle$ as a function of the vibrations' frequency ω (y axis) and of the amplitude a (x axis). The hotter the color the higher is the current.

where M_1, M_2, M_3, and M_4 are $(2N + 1) \times (2N + 1)$ matrices with the following components:

$$M_1(n, m) = i^m J_{m+n}(iK_m a)[C(-1)^{m+n+1} - D], \quad (18)$$

$$M_2(n, m) = i^m J_{m+n}(iK_m a)\{C + D(-1)^{m+n}\}, \quad (19)$$

$$M_3(n, m) = i^m J_{m+n}(iK_m a)K_m[C(-1)^{m+n+1} + D], \quad (20)$$

$$M_4(n, m) = i^m J_{m+n}(iK_m a)\{K_m[-C + D(-1)^{m+n}]$$
$$-\lambda[C + D(-1)^{m+n}]\}, \quad (21)$$

respectively, $\mathbf{V}_1$ and $\mathbf{V}_2$ are column vectors with the $2N + 1$ coefficients:

$$\mathbf{V}_1(n) = J_n(iK_0 a)[C + D(-1)^n], \quad (22)$$

$$\mathbf{V}_2(n) = K_0 J_n(iK_0 a)[-C + D(-1)^n], \quad (23)$$

respectively, and $\mathbf{r}$ and $\mathbf{t}$ are column vectors with the $2N + 1$ coefficients r_m and t_m, respectively.

Using these notations, the reflection and transmission coefficients can easily be derived by solving (17):

$$\begin{bmatrix} \mathbf{r} \\ \mathbf{t} \end{bmatrix} = \begin{bmatrix} M_1 & M_2 \\ M_3 & M_4 \end{bmatrix}^{-1} \begin{bmatrix} \mathbf{V}_1 \\ \mathbf{V}_2 \end{bmatrix}. \quad (24)$$

Once t_m is in hand [after solving Eq. (24)], the wave function on the right side of the well ψ_r can easily be evaluated [Eq. (3)], and the current beyond the barrier is simply

$$\langle j \rangle = 2\text{Re} \sum_m \psi_r^*(L)k_m \psi_r(L) = \sum_m 2k_m|\psi_r|^2, \quad (25)$$

where the electron charge was taken to be $e = 1$ and the notation "Re" stands for the real part.

Figure 2 is a false-color presentation of the exact numerical solution of the normalized current, $\langle j \rangle/2k_0$ [Eq. (25)], as a function of the vibrations' frequency ω and the vibrations' amplitude a (both axes are presented in logarithmic scales).

The results reveal four different spectral regimes.

(1) *The adiabatic regime* $\omega < \omega_{ad}$. In this regime, the oscillations period is the longest timescale of the system. Therefore, the moving well cannot trap and move the incoming particle, because, by the time the well moves, the particle has enough time to tunnel outward.

The spectral width of the resonance depends on the distance from the well to the edges of the barrier; therefore, the spectral width of the resonance (ω_{sw}) depends on the perturbations' amplitude a:

$$\omega_{sw}(a) \approx U e^{-2\sqrt{U-\Omega}(L-a)}. \quad (26)$$

In Fig. 2, ω_{sw} [Eq. (26)] is shown with a dotted curve. When the amplitude goes to zero, the spectral width goes to $\omega_{ad} \equiv \omega_{sw}(a = 0) \cong U \exp(-2\sqrt{U - \Omega}L)$, which determines the boundary between the first (adiabatic) and the second spectral regions. In a stationary RT process, maximum current occurs when the well is located exactly at the center of the barrier; therefore, in the adiabatic regime, the current decreases when the oscillations' amplitude increases.

(2) *The intermediate regime* $\omega_{ad} < \omega < \omega_T$. In this regime, the adiabatic solution is invalid; however, the tendency of decreasing current as a function of amplitudes still holds but the decline is more moderate. ω_T is a critical frequency, above which the moderate decline turns into an abrupt one.

(3) *The critical regime* $\omega_T < \omega < \omega_r$. In the third regime ($\omega_T < \omega < \omega_r$) the frequency of the vibration ω exceeds the frequency ω_T, and the particle can be trapped and moved with the well. In this case, the particle's kinetic energy can be higher than the resonance's spectral width,

$$(a\omega)^2/4 > U \exp[-2\sqrt{U - \Omega}(L - a)], \quad (27)$$

in which case the particle cannot be trapped in the well any longer, and therefore the resonance effect is destroyed and the *current substantially decreases*. However, when the oscillation's amplitude increases even further ($a > 2/\lambda$), then eventually the spectral width of the resonance becomes higher than the kinetic energy of the trapped particles, and the resonance state can be partially recovered yielding a corresponding current increase.

The critical point where the maximum kinetic energy $(a\omega)^2/4$ is equal to the spectral width of the resonance is shown with a black dashed curve in Fig. 2. Beyond that point, the reduction in the current is clearly shown.

(4) *Selected suppressed resonant tunneling* $\omega > \omega_r$. The fourth regime occurs when the vibration's energy quanta are higher than the energy gap between the resonance energy and the barrier's potential height, i.e., $\omega > \omega_r(\omega_r = U - \Omega)$. In this case, for specifics vibrations' frequencies ω_m the current is suppressed.

Four regimes are marked and separated by horizontal lines: the first regime, $\omega < \omega_{ad}$; the second regime, $\omega_{ad} < \omega < \omega_T$; the third regime, $\omega_T < \omega < \omega_r$; and the fourth regime, $\omega_r < \omega$. Equation (26) is plotted with a black dotted curve, and Eq. (39) is plotted with a dashed curve. ω_{ad} is the minimum value of Eq. (26), ω_T is the minimum value of Eq. (39) [i.e., Eq. (40)] and $\omega_r = U - \Omega$. The parameters are the barrier width $2L\sqrt{U} = 30$ and the incoming energy $\Omega = U - \lambda^2/4 + \eta$ where $\lambda/\sqrt{U} = 1$ and $\eta/U = 1.5 \times 10^{-7}$.

In what follows, we will discuss and investigate each of these spectral regions.

III. THE ADIABATIC REGIME

The adiabatic solution of Eq. (1) can be written in the following form:

$$\psi_r(x,t) = \psi_h(x,t) + \frac{\lambda \varphi_{\Omega+m\omega}^+(x_0) e^{-i(\Omega+m\omega)t}}{1 - \lambda G_{\Omega+m\omega}^+(x_0,x_0)} G_{\Omega+m\omega}^+(x,x_0),$$

(28)

where $\psi_h(x,t) = \phi_{\Omega+m\omega}^+(x) e^{-i(\Omega+m\omega)t}$ is the incoming homogenous solution and $G_{\Omega+m\omega}^+(x,x_0)$ is the outgoing Green function, which solves the equation

$$\delta(x-x_0) = -\frac{\partial^2}{\partial x^2} G_{\Omega+m\omega}^+(x,x_0)$$
$$+ [U(x) - (\Omega+m\omega)] G_{\Omega+m\omega}^+(x,x_0) \quad (29)$$

with the boundary conditions

$$G_{\Omega+m\omega}^+(x,x_0) \sim \exp(i\sqrt{\Omega+m\omega}|x-x_0|) \text{ for } |x| \to \infty.$$

(30)

Therefore, the outgoing Green function reads

$$G_{\Omega+m\omega}^+(x,x_0) = \begin{cases} \frac{\varphi_{\Omega+m\omega}^-(x_0)\varphi_{\Omega+m\omega}^+(x)}{\varphi_{\Omega+m\omega}^+(x_0)\varphi_{\Omega+m\omega}^{'-}(x_0)-\varphi_{\Omega+m\omega}^-(x_0)\varphi_{\Omega+m\omega}^{'+}(x_0)} & \text{for } x > x_0 \\ \frac{\varphi_{\Omega+m\omega}^-(x)\varphi_{\Omega+m\omega}^+(x_0)}{\varphi_{\Omega+m\omega}^+(x_0)\varphi_{\Omega+m\omega}^{'-}(x_0)-\varphi_{\Omega+m\omega}^-(x_0)\varphi_{\Omega+m\omega}^{'+}(x_0)} & \text{for } x < x_0 \end{cases}, \quad (31)$$

where again, $x_0 \equiv a\cos(\omega t)$ is the moving location of the well.

For $x > x_0$ Eq. (28) can be rewritten

$$\psi_r(x > x_0, t) = \frac{\varphi_{\Omega+m\omega}^+(x) e^{-i(\Omega+m\omega)t}}{1 - \lambda G_{\Omega+m\omega}^+(x_0,x_0)},$$

(32)

where the Green function at x_0 is

$$G_{\Omega+m\omega}^+(x_0,x_0) = \left[\frac{\varphi_{\Omega+m\omega}^{'-}(x_0)}{\varphi_{\Omega+m\omega}^-(x_0)} - \frac{\varphi_{\Omega+m\omega}^{'+}(x_0)}{\varphi_{\Omega+m\omega}^+(x_0)}\right]^{-1}, \quad (33)$$

and the mean current density is

$$\langle j \rangle = \frac{\omega}{2\pi} \int_0^{2\pi/\omega} 2\mathrm{Im}\left\{\psi_r^* \frac{\partial \psi_r}{\partial x}\right\} dt, \quad (34)$$

where "Im" stands for the imaginary part.

After substituting Eqs. (9)–(13) into (32) and into (34), the mean current can be written

$$\langle j \rangle = \frac{\omega}{2\pi} \int_0^{2\pi/\omega} \frac{2k|F|^2}{\left|A + \frac{B}{\mathrm{sech}[2Ka\cos(\omega t)]}\right|^2} dt, \quad (35)$$

where $K = \sqrt{U-\Omega}$, $k = \sqrt{\Omega}$ and $A \equiv 1 - \frac{\lambda(C^2+D^2)}{2K(C^2-D^2)}$, $B \equiv \frac{-\lambda CD}{K(C^2-D^2)}$.

Except for very small amplitudes, the coefficient A is significantly smaller than $B/\mathrm{sech}[2Ka\cos(\omega t)]$ and the current can be approximated by

$$\langle j \rangle \approx C\frac{\omega}{2\pi} \int_0^{\frac{2\pi}{\omega}} \mathrm{sech}^2[z\cos(\omega t)] dt,$$

where $C \equiv \frac{2k|F|^2}{|B|^2}$, $z \equiv 2Ka$.

When the energy of the incoming particle is equal to the resonance energy, which is the case under study, the probability to penetrate the barrier is very high, $|\psi_r|^2 \to 1$, in which case the maximum adiabatic current density is $2k$ and the coefficient C should be replaced with $C = 2k$; i.e., the

current reduces to simply

$$\langle j \rangle \approx k\frac{\omega}{\pi} \int_0^{2\pi/\omega} \mathrm{sech}^2[z\cos(\omega t)] dt. \quad (36)$$

The solution of the integral can be achieved using different approximations for $z > 1$ and for $z < 1$. In these regimes, the integral can be approximated by

$$k\frac{\omega}{\pi} \int_0^{2\pi/\omega} \mathrm{sech}^2[z\cos(\omega t)] dt$$
$$\cong \begin{cases} 2k\frac{(z^2+4)}{\sqrt{2}(z^2+2)^{3/2}} & \text{for } z < 1 \\ 4k[I_0(2z) - L_0(2z)] & \text{for } z > 1 \end{cases}, \quad (37)$$

where I_0 is the modified Bessel function and L_0 is the modified Struve function [43]. In Fig. 3 the exact numerical evaluation (as well as its analytical approximations) of the adiabatic current as a function of the vibrations' amplitude is plotted.

As can be seen from this figure, the reduction in the current is very large even for very small vibration amplitudes (the FWHM, in this case, is about $a/L \approx 0.1$). Moreover, it is clear from Fig. 3 that the analytical expressions (37) are a very good approximation for the exact adiabatic solution.

One of the most important characters of the first regime is that the average current density is *independent* of the vibration's frequency.

IV. THE INTERMEDIATE REGIME

The second regime is defined between ω_{ad} and ω_T (see Fig. 2). The lower limit of this spectral regime is determined by the minimum value of the resonance's spectral width $\omega_{sw}(a) = U\exp[-2\sqrt{U-\Omega}(L-a)]$, i.e., $\omega_{ad} = \omega_{sw}(0)$. Therefore, the second region is characterized by the property that the well's spatial movement is quicker than the characteristic escape time from the well. Therefore, the particle in this regime is at least partially moving with the well.

The upper limit of this region is the frequency ω_T, which will be discussed in detail in the next section.
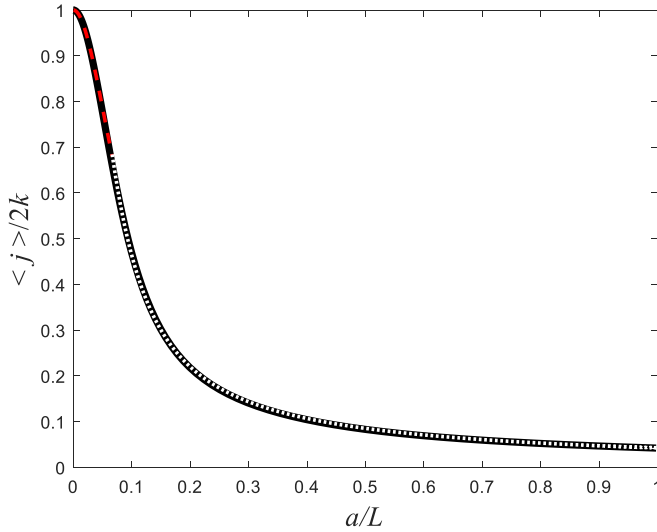
FIG. 3. The adiabatic current as a function of the vibrations' amplitude is plotted. The black curve is the exact numerical solution, while the dashed curve and the dotted one represent the analytical approximations for $z < 1$ and $z > 1$, respectively. In this case, the vibration frequency is $\frac{\omega}{U} = 10^{-9}$, and the other parameters are as in Fig. 2.

In Fig. 4 the mean current as a function of the vibration's amplitude is presented for three different values of the vibration's frequency in the second regime: $(e^{-15} \approx 3 \times 10^{-7}) < \omega/U < (e^{-6.5} \approx 1.5 \times 10^{-3})$.

Unlike the first spectral regime, here we see that the mean current is frequency dependent, and the higher the vibration's frequency, the more moderate is the decline.
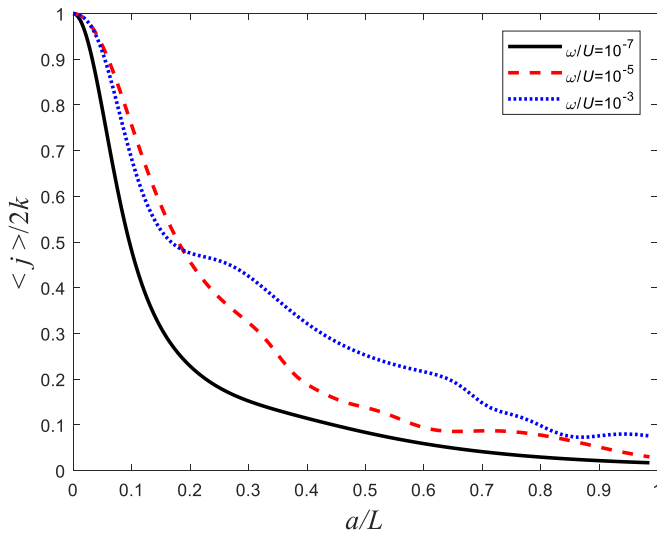

FIG. 4. The current as a function of the vibrations' amplitude is plotted for three different frequencies. The solid curve represents the lower limit $\omega \cong \omega_{ad}$, the dotted curve represents the upper limit (using the numeric results), and the dashed curve represents the center of the second regime $\omega = \sqrt{\omega_{ad}\omega_T} \approx 10^{-5}$. The other parameters are as in Fig. 2.
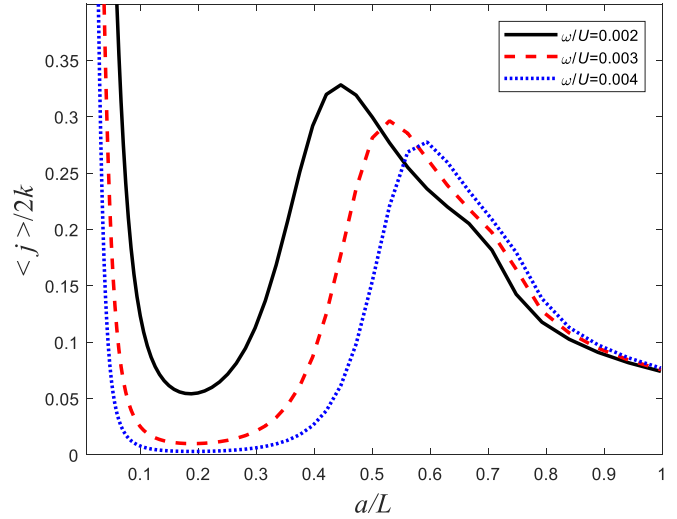

FIG. 5. The current as a function of the amplitude for three different frequencies within the third regime where $\omega_T < \omega < \omega_r$. The other parameters are as in Fig. 2.

V. THE CRITICAL REGIME

In the third regime, when the frequency of the vibration is even higher, $\omega > \omega_T$ (see Fig. 2), and the vibration's amplitude is small, the particle is trapped to the well and vibrates with it. In this case, the particle is trapped since the vibration's frequency is larger than the tunneling rate. Consequently, RT is kept and the current is high.

However, when the kinetic energy of the trapped particle exceeds the spectral width of the resonance, then the resonance state cannot keep the particle trapped any longer, and consequently, the particle escapes from the well and the current decreases substantially.

The maximum kinetic energy of the vibrating trapped particle is $(a\omega)^2/4$. Therefore, the critical frequency, beyond which current reduction occurs, should obey

$$(a\omega)^2/4 = U \exp[-2\sqrt{U - \Omega}(L - a)]. \qquad (38)$$

Since at the resonance $\Omega = U - \lambda^2/4$, the critical frequency is equal to

$$\omega_c(a) = \frac{2\sqrt{U}}{a} e^{-\frac{\lambda}{2}(L-a)}. \qquad (39)$$

Equation (39) is shown with the dashed curve in Fig. 2, and indeed beyond this critical frequency, the current experienced a rapid decline.

The transition frequency [Eq. (39)] is the main result of this paper since it exhibits an abrupt transition between high and low current. We have presented this phenomenon for harmonic vibrations, but there is no reason to expect that this conduct will not occur for different kinds of oscillations.

In fact, it shows that the transition occurs whenever the kinetic energy of the bounded particle exceeds the spectral width of the bound state. This can occur in any kind of temporal dependence.

The third regime is presented in Figs. 5 and 6. In Fig. 5 three spectral scenarios are shown in linear axes. Figure 6 is similar to Fig. 2 where the focus is on the third regime.
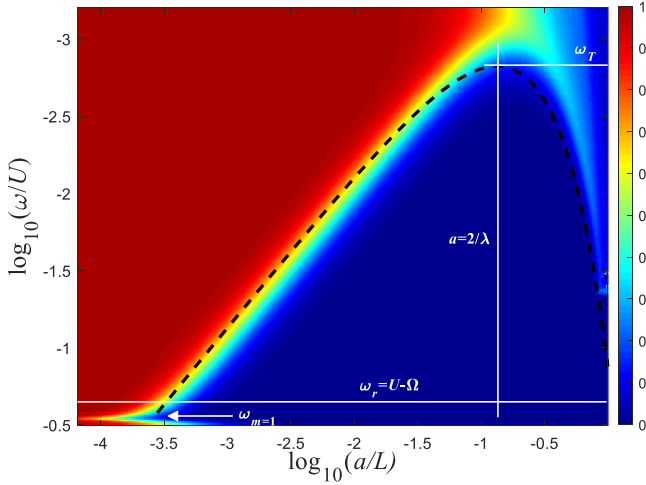
FIG. 6. The third regime $\omega_T < \omega < \omega_r$ is plotted (an enlargement of Fig. 2). The false-colors matrix represents the exact numerical solution. The frequencies ω_T [Eq. (40)] and ω_r are marked by white horizontal lines. Equation (39) is plotted with a black dashed curve. The parameters are as in Fig. 2.

One of the interesting features of this region is that when the oscillation's amplitude increases even further ($a > 2/\lambda$), then eventually the spectral width of the resonance becomes higher than the kinetic energy of the trapped particles. Consequently, the resonance state can be partially recovered, yielding a corresponding current increase, which is clearly seen in Figs. 5 and 6.

The minimum value of Eq. (39), $\min[\omega_c(a)] = \omega_T$, which determines the lower boundary of the third regime, occurs for $a = 2/\lambda$, in which case its value is

$$\omega_T = \omega_c(a = 2/\lambda) = \lambda \sqrt{U} e^{1 - \frac{\lambda L}{2}}. \qquad (40)$$

When the vibration's frequency increases beyond this value (40) the solution of Eq. (39) splits into two solutions. For a relatively high frequency, the gap between the low-amplitude solution $a \cong 2\sqrt{U}/\omega \exp(-\lambda L/2)$ and the high-amplitude one ($a \cong L$) increases substantially. The upper limit of the third regime is the frequency: $\omega_r = U - \Omega$, where the vibration frequency is of the same order as the potential gap.

VI. SELECTED SUPPRESSED RT

We have seen that as the oscillation's frequency increases the maximum vibration's amplitude should decrease to keep the particle in the quasiresonance state. This tendency continues as long as the oscillation's energy quantum is lower than the barrier's gap $\omega \ll U - \Omega$. When ω is of the same order as the barrier gap, the trapped electron can absorb a single energy quantum ω and escapes from its quasiresonance level. Consequently, the resonant effect is destroyed and the current decreases.

However, in practice, the particle can easily escape from its quasiresonance state only when its final energy is equal to
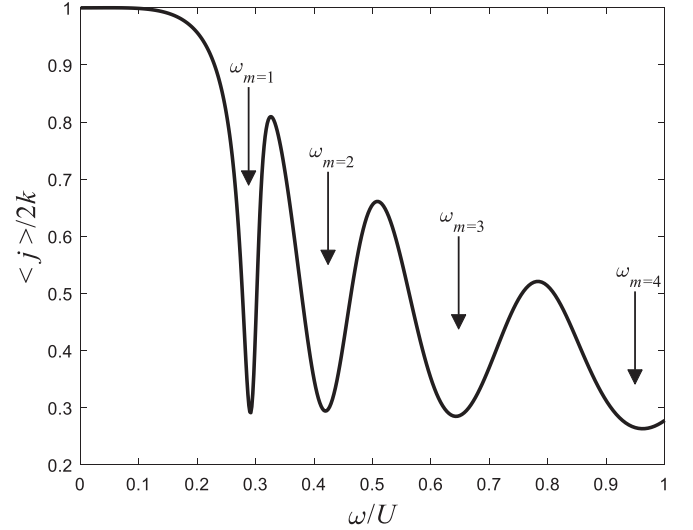

FIG. 7. The exact solution of the mean current density as a function of the vibrations' frequency ω. The suppression frequencies ω_m [Eq. (42)] are denoted by arrows. In this case $a/L = 0.0002$. The other parameters are as in Fig. 2.

the quasiresonance state *above* the barrier, i.e., only when the *final*, the activation, energy, is equal to

$$\Omega_m = U + \frac{m^2 \pi^2}{L^2}, \quad m = 1, 2, 3 \ldots, \qquad (41)$$

which means that current suppression occurs at the oscillation frequencies:

$$\omega_m = U - \Omega + \frac{m^2 \pi^2}{L^2}, \quad m = 1, 2, 3 \ldots. \qquad (42)$$

It should be noted that due to the presence of the δ function at (approximately) the center of the barrier, only the antisymmetric quasistates are relevant to current suppression (the symmetric quasiresonance states,

$$\Omega_m = U + \frac{m^2 \pi^2}{4L^2}, \quad m = 1, 2, 3, \ldots,$$

are not allowed, in which cases the particle is kept in the moving well and the current increases due to resonant tunneling).

In Fig. 7 the current as a function of the vibrations' frequency ω is plotted for a given vibration's amplitude. The first four suppression frequencies ω_m are marked by vertical arrows. The first three suppression frequencies are shown with white arrows in Fig. 2. Figure 8 is an enlargement of the fourth regime of Fig. 2.

Unlike the other three regimes, where the mean energy of the tunneling particle remains unchanged, i.e., $\Omega_{\rm act} \approx \Omega$, in the fourth regime, the tunneled particle absorbs a single phonon (oscillating quantum) and exists the barrier with higher energy $\Omega_{\rm act} = \Omega + \omega > U$.

VII. DISCUSSION

In the third regime, the tunneling current strongly depends on the vibration frequency ω and on the amplitude a, and
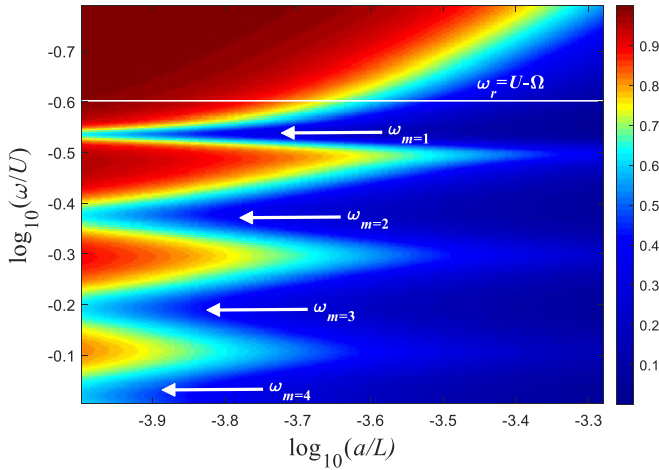
FIG. 8. The fourth regime $\omega > \omega_r$ is plotted (an enlargement of Fig. 2.) The colored matrix represents the exact numerical solution. The frequency ω_r is shown in a white line. The suppression frequencies ω_m are marked with horizontal arrows. The parameters are as in Fig. 2.

therefore is extremely sensitive to the acceleration of the vibrating well. This effect can be used to design extremely sensitive accelerometers.

An accelerometer device is depicted in Fig. 9. The device measures the tunneling current through a metal capacitor, where a nanometric metal plate is introduced between its plates. The nanoplate can be regarded as a quantum dot, which is connected to an insulating cantilever. The oscillating nanoplate is presented by the oscillating well in our model, and the barrier represents the air between the plates. The cantilever's elasticity and the plate's mass determine the device's mechanical oscillating frequency ω. Therefore, the amplitude of the plate's oscillations (a) determines the linear acceleration $\alpha = a\omega^2$. In some respects, this device can be regarded as a scanning tunneling microscope, where the vibrations of the tip are measured using a capacitor (capacitors are common in modern accelerometers; see, for example [44–46]).

Using Eq. (39) the device's precision can be evaluated. Since the critical frequency depends exponentially on the
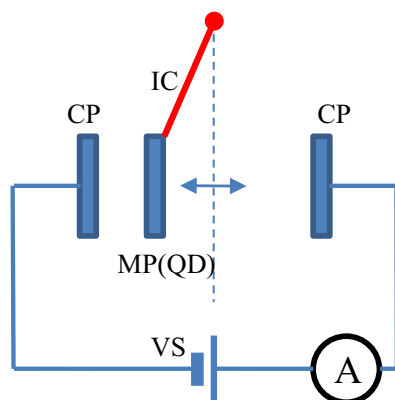

FIG. 9. System schematic. CP is the capacitor's plates, IC is the insulating cantilever, MP(QD) is the nano-metal plate (quantum dot), VS is the voltage source, and A represents the microammeter.

TABLE I. Capacitive accelerometer.

2L [nm]	a [pm]	f [Hz]	Precision in acceleration (in g) for 0.1% current change
12	2.0	3200	8.3×10^{-8}
13	1.8	320	8.0×10^{-10}
14	1.3	32	5.4×10^{-12}

distance between the capacitor's plates (2L), the device's sensitivity can be arbitrarily high. To illustrate this sensitivity, some values are presented in Table I for the values $U \cong 4\,\mathrm{eV}$ (which is a standard value in STM metals [47,48]) and $\Omega \cong 3\,\mathrm{eV}$. In Table I the accuracy in acceleration measurement is presented as a function of the distance between the capacitor plates (2L) and the accuracy in the current measurement. The acceleration accuracy is measured in mean gravity of earth $g = 9.8\,\mathrm{m/s}^2$.

Since the slope of the current as a function of the acceleration at the transition region is inversely proportional to the acceleration, then 0.1% accuracy in current measurement corresponds approximately to 0.001α in acceleration accuracy, when α stands for the acceleration at the transition. The wider the distance between the plates and the better the current's measurements, the better is the accelerometer's accuracy. As can be seen from Table I, this device can be used to measure minuscule accelerations (as low as pico g's).

On the other hand, the wider the distance, the more accurate the electrons' energy must be (since the resonant energy becomes exponentially narrower). Consequently, the current may decrease below noise level, which is missing in these ideal calculations.

Another accelerometer device is presented in Fig. 10. In this optical device, atoms of rubidium (Rb) tunnel between three optical traps (optical tweezers). The central optical trap oscillates with frequency f and amplitude a, according to Eq. (39).

In the left panel of Fig. 10(a), the oscillations' amplitude is small and the Rb atoms can tunnel from the left to the right traps via the oscillating one. In the right panel Fig. 10(b) the vibrations exceed the critical value and the tunneling decreases substantially.
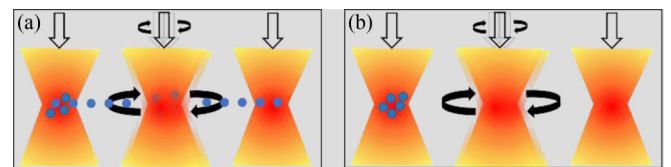

FIG. 10. Optical accelerometer schematic. Initially, Rb atoms are trapped in the left optical trap. When the center's trap accelerations are below the critical value, the atoms can tunnel toward the right trap (a); however, when these accelerations exceed this value, tunneling is frustrated (b).

TABLE II. Optical accelerometer.

$2L$ [μm]	a [nm]	f [KHz]	Precision in acceleration (in g) for 0.1% current change
3	20	2.7	5.9×10^{-4}
5	20	1.1	9.2×10^{-5}
7	20	0.4	1.4×10^{-5}

The acceleration measurements' accuracy of a typical device is presented in Table II. In this case, $2L$ represents the distance between the left and the right traps. The wider the distance between the traps and the better the current's measurements, the better is the accelerometer's accuracy. In Table II the barrier height was chosen to be ~10 nK.

VIII. SUMMARY

The resonant-tunneling current via a spatially oscillating potential well was calculated and investigated. It was found that this process consists of four different spectral regimes: (1) the adiabatic regime, where the particle has sufficient time to escape from the moving well; (2) the intermediate regime, where the particle partially remains within the well; (3) the trapping regime, where the particle is confined to the well, despite its movement; and (4) the activation regime, where the chances of activation to a quasiresonance level (and to lower the current) are frequency sensitive.

The main result of this paper is the third regime, where the oscillation frequency determines a maximum oscillation's amplitude, beyond which the velocity is too high to keep the particle in the trapping well. Consequently, the current decreases abruptly.

It should be stressed, that despite that this work's focus on a δ function well, the results are valid for any local moving well provided the incoming particles' energy is close to the well's resonant energy. Since scattering occurs between resonant states, the specific shape of the well is not important for the occurrence of the effect.

This effect can be implemented in extremely sensitive quantum accelerometers, where very small variations in the well's vibrations can have a large impact on the device's current.

Moreover, the resemblance of this model to an olfactory receptor may explain the receptor's sensitivity to the molecule's vibrations.

[1] E. Merzbacher, *Quantum Mechanics* (Wiley, New York, 1970).

[2] D. Bohm, *Quantum Theory* (Dover Publications, New York, 1989).

[3] M. Razavy, *Quantum Theory of Tunneling* (World Scientific, Singapore, 2003).

[4] L. D. Landau and E. M Lifschitz, *Quantum Mechanics* (Pergamon, Oxford, 1976), Sec. 46.

[5] B. Ricco and M. Ya. Azbel, Physics of resonant tunneling. The one-dimensional double-barrier case, Phys. Rev. B **29**, 1970 (1984).

[6] E. Granot, Point scatterers and resonances in low number of dimensions, Physica E **31**, 13 (2006).

[7] M. Y. Azbel, Eigenstate Assisted Activation, Phys. Rev. Lett. **68**, 98 (1992).

[8] M. Y. Azbel, Elevator resonance activation, Europhys. Lett. **18**, 537 (1992).

[9] M. Buttiker and R. Landauer, Traversal Time for Tunneling, Phys. Rev. Lett. **49**, 1739 (1982).

[10] G. Kalbermann, Assisted tunneling of a metastable state between barriers, Phys. Rev. C **77**, 041601(R) (2008).

[11] E. Granot, Selected elevation in quantum tunneling, Europhys. Lett. **61**, 817 (2003).

[12] E. Granot, Forbidden activation levels in a non-stationary tunneling process, Physica E **14**, 397 (2002).

[13] G. Zangwill and E. Granot, Eigenstate suppressed activation, Physica B **461**, 140 (2015).

[14] E. Granot and G. Zangwill, Dynamic resonant tunneling, in *Quantum Dynamics*, edited by P. Bracken (InTech, Rijeka, Croatia, 2016), p. 55.

[15] M. Belloni and R. W. Robinett, The infinite well and Dirac delta function potentials as pedagogical, mathematical and physical models in quantum mechanics, Phys. Rep. **540**, 25 (2014).

[16] E. Granot, The tunneling current through oscillating resonance and the Sisyphus effect, Adv. Cond. Matter Phys. **2017**, 2435857 (2017).

[17] K. K. Ng, *Complete Guide to Semiconductor Devices*, 2nd ed. (John Wiley & Sons, New York, 2010).

[18] W. Z. Bao, F. Miao, Z. Chen, H. Zhang, W. Jang, C. Dames, and C. N. Lau, Controlled ripple texturing of suspended graphene and ultrathin graphite membranes, Nat. Nanotechnol. **4**, 562 (2009).

[19] J. R. F. Lima, L. F. C. Pereira, and C. G. Bezerra, Controlling resonant tunneling in graphene via Fermi velocity engineering, J. Appl. Phys. **119**, 244301 (2016).

[20] C. Hwang, D. A. Siegel, S. K. Mo, W. Regan, A. Ismach, Y. Zhang, A. Zettl, and A. Lanzara, Fermi velocity engineering in graphene by substrate modification, Sci. Rep. **2**, 590 (2012).

[21] S. Chang, S. Huang, J. He, F. Liang, P. Zhang, S. Li, X. Chen, O. Sankey, and S. Lindsay, Electronic signatures of all four DNA nucleosides in a tunneling gap, Nano Lett. **10**, 1070 (2010).

[22] J. A. Fereiro, X. Yu, I. Pecht, M. Sheves, J. C. Cuevas, and D. Cahen, Tunneling explains efficient electron transport via protein junctions, Proc. Natl. Acad. Sci. USA **115**, E4577 (2018).

[23] S. Lloyd, Quantum coherence in biological systems, J. Phys.: Conf. Series **302**, 012037 (2011).

[24] L. Turin, A spectroscopic mechanism for primary olfactory reception, Chem. Senses **21**, 773 (1996).

[25] G. M. Dyson, The scientific basis of odour, J. Soc. Chem. Indus. **57**, 647 (1938).

[26] J. C. Brookes, F. Hartoutsiou, A. P. Horsfield, and A. M. Stoneham, Could Humans Recognize Odor by Phonon Assisted Tunneling? Phys. Rev. Lett. **98**, 038101 (2007).

[27] M. I. Franco, L. Turin, A. Mershin, and E. M. C. Skoulakis, Molecular vibration-sensing component in drosophila melanogaster olfaction, Proc. Natl Acad. Sci. USA **108**, 3797 (2011).

[28] R. D. Hoehn, D. Nichols, H. Neven, and S. Kais, Neuroreceptor activation by vibration-assisted tunneling, Sci. Rep. **5**, 9990 (2015).

[29] M. Horitani, A. R. Offenbacher, C. A. M. Carr, T. Yu, V. Hoeke, G. E. Cutsail III, S. Hammes-Schiffer, J. P. Klinman, and B. M. Hoffman, ^{13}C ENDOR spectroscopy of lipoxygenase-substrate complexes reveals the structural basis for C-H activation by tunneling, J. Am. Chem. Soc. **139**, 1984 (2017).

[30] S. Hay, L. O. Johannissen, P. Hothi, M. J. Sutcliffe, and N. S. Scrutton, Pressure effects on enzyme-catalyzed quantum tunneling events arise from protein-specific structural and dynamic changes, J. Am. Chem. Soc. **134**. 9749 (2012).

[31] E. K. Irish, R. Gómez-Bombarelli, and B. W. Lovett, Vibration-assisted resonance in photosynthetic excitation energy transfer, Phys. Rev. A **90**, 012510 (2014).

[32] N. Pavlicek, I. Swart, J. Niedenfuhr, G. Meyer, and J. Repp, Symmetry Dependence of Vibration-Assisted Tunneling, Phys. Rev. Lett. **110**, 136101 (2013).

[33] W. J. Bruno and W. Bialek, Vibrationally enhanced tunneling as a mechanism for enzymatic hydrogen transfer, Biophys. J. **63**, 689 (1992).

[34] P. Rebentrost, M. Mohseni, I. Kassal, S. Lloyd, and A. Aspuru-Guzik, Environment-assisted quantum transport, New J. Phys. **11**, 033003 (2009).

[35] H. C. Liu, Resonant tunneling through single layer heterostructures, Appl. Phys. Lett. **51**, 1019 (1987).

[36] S. Geltman, Bound states in delta function potentials, J. At., Mol., Opt. Phys. **2011**, 573179 (2011).

[37] Z. Ahmed, S. Kumar, M. Sharma, and V. Sharma, Revisiting double Dirac delta potential, Eur. J. Phys. **37**, 045406 (2016).

[38] E. Demiralp and H. Beker, Properties of bound states of the Schrödinger equation with attractive Dirac delta potentials, J. Phys. A **36**, 7449 (2003).

[39] G. T. Camilo, F. A. Barone, and F. E. Barone, Interactions between delta-like sources and potentials, Phys. Rev. D **87**, 025011 (2013).

[40] D. F. Martinez and L. E. Reichl, Transmission properties of the oscillating δ-function potential, Phys. Rev. B **64**, 245315 (2001).

[41] J. Campbell, Some exact results for the Schrödinger wave equation with a time-dependent potential, J. Phys. A Math. Gen. **42**, 365212 (2009).

[42] D. C. Champeney, *Fourier Transforms and Their Physical Applications* (Academic Press, New York, 1973).

[43] M. Abramowitz and A. Stegun, *Handbook of Mathematical Functions* (Dover Publications, New York, 1965).

[44] A. Beliveau, G. T. Spencer, K. A. Thomas, and S. L. Roberson, Evaluation of MEMS capacitive accelerometers, IEEE Design Test Comput. **16**, 48 (1999).

[45] D. K. Shaeffer, MEMS inertial sensors: A tutorial overview, IEEE Commun. Mag. **51**, 100 (2013).

[46] M. G. Guney, X. Li, V. P. J. Chung, J. Paramesh, T. Mukherjee, and G. K. Fedder, High dynamic range CMOS-MEMS capacitive accelerometer array, *Proceedings of the IEEE Micro electro mechanical Systems (MEMS) Conference*, Belfast, UK, Jan. 21-25, 2018 pp. 992–995.

[47] L. Giordano, F. Cinquini, and G. Pacchioni, Tuning the surface metal work function by deposition of ultrathin oxide films: Density functional calculations, Phys. Rev. B **73**, 045414 (2006).

[48] J. Wintterlin, J. Wiechers, H. Brune, T. Gritsch, H. Hofer, and R. J. Behm, Atomic-Resolution Imaging of Close-Packed Metal Surfaces by Scanning Tunneling Microscopy, Phys. Rev. Lett. **62**, 59 (1989).